INCREASED ARTERY WALL STRESS POST-STENTING LEADS TO GREATER INTIMAL THICKENING

Lucas H. Timmins[1], **Matthew W. Miller**[2,4], **Fred J. Clubb Jr.**[3,4], and **James E. Moore Jr.**[1,4]

[1] Department of Biomedical Engineering, Texas A&M University, College Station, TX, USA 77843-3120

[2] Department of Small Animal Clinical Sciences, Texas A&M University, College Station, TX, USA 77843-4474

[3] Department of Veterinary Pathobiology, Texas A&M University, College Station, TX, USA 77843-4467

[4] M. E. DeBakey Institute, Texas A&M University, College Station, TX, USA

Abstract

Since the first human procedure in the late 1980s, vascular stent implantation has been accepted as a standard form of treatment of atherosclerosis. Despite their tremendous success, these medical devices are not without their problems, as excessive neointimal hyperplasia can result in the formation of a new blockage (restenosis). Clinical data suggest that stent design is a key factor in the development of restenosis. Additionally, computational studies indicate that the biomechanical environment is strongly dependent on the geometrical configuration of the stent, and therefore possibly involved in the development of restenosis. We hypothesize that stents that induce higher stresses on the artery wall lead to a more aggressive pathobiologic response, as determined by the amount of neointimal hyperplasia. The aim of this investigation was to examine the role of solid biomechanics in the development of restenosis. A combination of computational modeling techniques and in vivo analysis were employed to investigate the pathobiologic response to two stent designs that impose greater or lesser levels of stress on the artery wall. Stent designs were implanted in a porcine model (pigs) for approximately 28 days and novel integrative pathology techniques (quantitative micro-computed tomography, histomorphometry) were utilized to quantify the pathobiologic response. Concomitantly, computational methods were used to quantify the mechanical loads that the two stents place on the artery. Results reveal a strong correlation between the computed stress values induced on the artery wall and the pathobiologic response; the stent that subjected the artery to the higher stresses had significantly more neointimal thickening at stent struts (high stress stent: 0.197 ± 0.020 mm vs. low-stress stent: 0.071 ± 0.016 mm). Therefore, we conclude that the pathobiologic differences are a direct result of the solid

Correspondence: James E. Moore, Jr., Ph.D., Department of Biomedical Engineering, Texas A&M University, 337 Zachry Engineering Center, College Station, TX 77843-3120, jmoorejr@tamu.edu, Phone: (979)845-3299, Fax: (979)845-4450.

biomechanical environment, confirming the hypothesis that stents that impose higher wall stresses will provoke a more aggressive pathobiological response.

Keywords

biomechanics; finite element method; pathobiology; restenosis; vascular stent; vascular pathology

Despite the technological advances since the first human implantation of a vascular stent, the development of neointimal tissue following implantation of these devices still remains an incessant problem for the treatment of atherosclerosis. Neointimal hyperplasia can ultimately lead to device failure due to the development of a new blockage (restenosis) in the stented region. Clinical data have indicated the significance of stent design in the formation of neointimal tissue. Restenosis rates in coronary arteries ranging from approximately 20 – 40% for bare metal stents (BMS) have been reported, with the BMS differing only by their geometrical configuration (1, 2). While drug-eluting stents (DES) have decreased restenosis rates to < 10% in coronary applications (2), numerous problems [e.g. late stent thrombosis (3), impaired reendothelialization (3), failure in peripheral arteries (4), hypersensitivity reactions (5)] and high cost have raised concerns over their exclusive use. Regardless of the failure rates of these devices, in 2006 alone, more than 650,000 percutaneous coronary interventions coupled with stent implantation were performed (6). This number does not include the number of stent implantations in other areas of the vasculature (e.g. carotid, renal, femoral). Thus, since vascular stenting is a standard for treatment of occlusive artery disease, and their use is likely to increase, there is an imperative need to increase the success rate of this therapy.

The biological mechanisms that result from the introduction of a stent into the vasculature have been investigated in both humans and animal models. Edelman and Rogers (7) defined the vascular response to stenting as a four-phase process (thrombosis, inflammation, proliferation, and remodeling) that may or may not result in restenosis. Previous investigations suggests that biomechanics plays a key role in each of these pathobiologic stages. Moreover, the biomechanical impact of stents is largely governed by their exact design configuration.

The first phase in the response of the artery wall to stent implantation is thrombus formation. This involves the aggregation of platelets to the partially denuded artery wall and stent struts, both of which can be highly thrombogenic surfaces. The degree to which platelets adhere to these surfaces depends primarily on whether or not the local flow field is directed toward or away from the wall (8). Higher degrees of platelet aggregation have been noted in regions where instantaneous streamlines point toward the wall. One result of this behavior is that in areas where stent struts are very closely packed, and the mainstream of the flow "skims over" the top of the stagnant area in between, platelet aggregation is lowest (9). Presumably, delivery of blood-borne inflammatory cells follows similar patterns. Platelets and inflammatory cells can also be triggered into their activated states by stagnant flow patterns and in particular, low shear-stress values (10, 11). The altered solid mechanical environment following stent deployment also governs the inflammatory and remodeling

response. In vivo and in vitro studies have demonstrated that arterial adventitial fibroblasts migrate to the neointima where they differentiate into myofibroblasts and secrete various extracellular matrix proteins (12, 13). This migratory response is a direct result of the mechanical forces induced on the artery wall following stent implantation. Computational studies have shown that the solid mechanical environment is strongly dependent on stent design. In particular, stents that are characterized by a large strut spacing and axial amplitude, defined as the distance between the peaks and troughs of a repeating sinusoidal stent ring segment, impose considerably less stress on healthy (14), tapered (15), and diseased artery models (16). Thus, there is a tremendous body of evidence indicating that stent design plays a significant role in the altered fluid and solid mechanical environments following their deployment, and it is reasonable to expect that the overall mechanical environment affects the long-term patency of these devices. Further information on the effects of specific stent design parameters on in vivo responses and especially the eventual development of intimal hyperplasia would be of benefit in designing more successful implantable devices.

There is a clear role of biomechanics in the improvement of currently available vascular stents and in their future development. It is interesting to note that many DES essentially employ the same design configuration as their BMS counterparts with a drug-loaded polymer coating on the underlying metallic surface (e.g. Cypher and Bx Velocity, Cordis, Johnson & Johnson, Miami Lakes, FL, USA; TAXUS and NIR, Boston Scientific Corp., Natick, MS, USA). These similarities have lead to some concern over the long-term effect of DES following complete elution of the drug. Recently the PAINT trial compared the effectiveness of three geometrically identical stents [one BMS and two DES that were covered with an identical biodegradable-polymer carrier releasing either paclitaxel or sirolimus (17)]. While results revealed a significant difference in the in-stent and in-lesion restenosis rates between either DES when compared to the BMS, there was no significant difference when comparing results between the two DES. Applying such findings to clinical trials that examine two commercially available stents that do vary in design [e.g. CypherR Sirolimus-eluting Coronary Stent (Cordis), TAXUSR Liberte® Paclitaxel-eluting Coronary Stent System (Boston Scientific)], indicate that the difference in restenosis rates between these stents might not be a difference in their loaded cytostatic drugs, but rather differences in stent designs.

As a means of correlating the biomechanical environment and resulting pathobiological response following stent implantation of various designs, we employed a combination of computational modeling techniques and in vivo analysis to directly assess the role of biomechanics in the development of restenosis. In particular, our main objective in this study was to provide a rationale for the observed clinical differences in restenosis rates between stent designs. Specifically, we were interested to know if stents whose geometric designs induce higher stresses on the artery wall result in a greater volume of neointimal tissue. As such, we quantified both the solid biomechanical environment and in vivo arterial response of two stent designs that have been shown to impose considerably different mechanical stresses and strains on the arterial wall. We tested the hypothesis that stents that induce a non-favorable biomechanical environment (i.e. subject the artery to higher non-physiologic stresses) provoke a more aggressive pathobiological response of the artery wall,

resulting in a higher degree of neointimal hyperplasia. The results from this investigation will provide insight into the design of vascular stents that reduce the mechanical trauma on the artery wall, and thereby reduce the neointima hyperplasia and increase the success rates of future stent design iterations.

Materials and Methods

To examine the pathobiologic response to vascular stent designs that induce extremely different biomechanical environments, two stent designs were deployed in a healthy porcine model. Similar stent designs were investigated previously using the finite element (FE) method (14–16) and shown to induce either extremely high or low stresses on the arterial wall; herein, the two designs investigated are denoted as the high-stress and low-stress stent designs, respectively (Fig. 1). Computational modeling techniques were used to examine the mechanical loads induced by the two stent designs on a 3-dimensional (3D), healthy, thick-walled, non-linear model of the artery wall. In addition, quantitative evaluation of the pathobiologic response was achieved by utilization of integrative pathology techniques [quantitative micro-computed tomography (CT), histomorphometry].

Computational Modeling

The computational modeling techniques have been employed and discussed in detail elsewhere (14–16, 18). Briefly, the computer-aided design drawings provided to Laserage Technology Corporation (Waukegan, IL, USA) for cutting of the stents were imported into MSC.Patran (MSC Software, Santa Ana, CA, USA) to create 3D finite element models of the stented arteries. Characterized by design parameters previously defined (14), the high-stress stent had a strut spacing, radius of curvature, and axial amplitude of 1.50, 0.02, and 1.44 mm, respectively, while the low-stress stent had values of 3.05, 0.07, and 3.13 mm, respectively (Fig. 1). Total stent to artery surface area ratio was 0.22 and 0.10 for the high-stress and low-stress designs, respectively. Stent designs had a constant strut thickness of 100 μm and a deployed outer radius of 2.5 mm. The high-stress stent had a strut cross-sectional area (CSA) of 0.015 mm^2 in the struts that composed the repeating sinusoidal ring segments and a CSA of 0.01 mm^2 in the struts that connected the ring segments, while the low-stress stent had a constant strut CSA of 0.01 mm^2 throughout the stent (all measurements required for manufacturing purposes). Furthermore, the high-stress stent had free cell areas of either 4.68 or 6.00 mm^2, while the low-stress stent had free cell areas of either 10.49 or 15.29 mm^2. Note that the free cell areas differed due to the odd number of peaks in the repeating sinusoidal rings of the stent designs and are within the range of values reported for commercially available designs (19). The stent material was modeled as 316L stainless steel ($E = 200$ GPa, $\nu = 0.3$).

The artery was modeled as a straight homogenous cylinder with isotropic nonlinear hyperelastic material properties that were determined from biaxial mechanical testing of porcine arterial tissue as previously described (14). Dimensions of the artery model were determined from average measurements of all hematoxylin and eosin (H&E) stained histological sections [inner unloaded radius (ρ_i), outer unloaded radius (ρ_o)] and from angiographic data [loaded inner radius (r_i)] obtained during stent implantation (discussed

below). Assuming that arterial tissue is an incompressible material, which has been quantified experimentally (20), the loaded outer radius (r_o) value was determined by

$$r_o = \sqrt{r_i^2 + \frac{1}{\lambda_z}(\rho_o^2 - \rho_i^2)}$$

where λ_z is the axial stretch ratio. The axial stretch ratio was assumed to be 1.57, which agrees with experimental measurements obtained from the most distal end of porcine aortas just proximal to the iliac bifurcation (21). As a result, the inner and outer radii values of the artery model at diastolic pressure were 1.72 (agrees with angiographic data) and 1.94 mm, respectively.

To determine the differences in the mechanical impact of implanting the two stent designs, the biomechanical environment induced on the artery wall was analyzed. In particular, circumferential (hoop) wall stress and radial displacement values on the inner surface of the artery wall were evaluated. Both parameters were examined at diastolic pressure, as it is during this part of the cardiac cycle where the mechanical impact of stenting is most severe (i.e. the stent is stretching the artery in the radial direction the greatest and stresses are highest). Circumferential wall stresses were analyzed as they are most likely to disrupt and possibly rupture the internal elastic lamina (IEL), which has been shown experimentally to be directly associated with the development of restenosis (22, 23). Furthermore, previous analysis in our lab has indicated that circumferential stress constitutes the major contribution in the maximum principal stresses. Thus, only circumferential stress values on the intimal surface of the artery are presented herein. As a reference, the Law of Laplace estimates the circumferential wall stress to an unstented artery with identical geometric dimensions as approximately 83 kPa at diastolic pressure. While this formula is not appropriate in this situation [i.e. the Law of Laplace is only applicable in determining the circumferential (Cauchy) stress in a thin-walled pressurized cylinder], the value serves as a general reference guideline for evaluation of the extremely high non-physiologic, stent induced stress values placed on the artery wall. Radial displacement values on the inner surface of the artery were also analyzed as a means of assessing the ability of the stents to maintain a patent lumen following implantation (i.e. they provide enough radial rigidity to prevent elastic recoil by the artery).

Quantitative analysis of the FE models was achieved by evaluation of nodal values for circumferential stress and radial displacement. The nodal values were either plotted as color maps to assess the stress and displacement fields or exported for further post-processing (e.g. determining average values in the stented regions) in Matlab (MathWorks, Natick, MS, USA) subroutines. To assess the convergence of the FE mesh, element mesh densities on the artery wall were independently doubled in all principal directions (r, θ, z), and simulations, as described above, were carried out. The mesh was deemed converged when maximum circumferential stress and radial displacement values on the intimal surface of the stented region differed by < 4.5 and $\ll 1$ %, respectively, at diastolic pressure.

Animal Model

All surgeries were performed in the catheterization suite in the Texas A&M Small Animal Clinic (College of Veterinary Medicine and Biomedical Sciences, Texas A&M University, College Station, TX). The Institutional Animal Care and Use Committee at Texas A&M University approved animal experimental procedures.

Prior to surgery, an initial pre-operation examination, including deworming and baseline blood work, was carried out on healthy female domestic pigs (n = 8). Animals were started on dual-antiplatelet therapy (e.g., aspirin, Plavix) seventy-two hours prior to surgery (once daily), and this therapy was continued post-op until explants. Heparin (300 units/kg) was administered intravenously to prevent acute stent thrombosis. Following isolation of the left common carotid artery, an 8 F catheter introducer sheath was inserted into the artery using a modified Seldinger technique. Subsequently a guide wire and angiographic catheter were positioned in the distal aorta under fluoroscopy. Prior to stent implantation, the vascular of the hind limb was characterized with selective angiography to determine artery diameter and other anatomical features (e.g. branching, taper, etc.). Preliminary testing indicated that a stent-to-artery ratio of approximately 1.4:1.0 was required to ensure proper stent deployment (e.g. adequate strut apposition, no stent migration). Note that while this ratio is higher than that observed in clinical practice, no diseased tissue was present to contact the stent prior to maximum radial position. Furthermore, excessive injury was avoided as histopathologic examination revealed an intact internal elastic lamina (IEL) at all stent struts in most of the implants (discussed below). All images and videos were stored digitally. One stent design was deployed in the left common iliac (or common femoral) artery. The procedure was repeated in the contralateral iliac (or femoral) with deployment of the other stent design, such that one of each design was implanted in the left or right iliac (or femoral) artery. In the event that the vasculature allowed multiple stents to be deployed on each side (i.e. proper vessel diameter along sufficient length), a total of four stents were deployed (1 stent of each design in each side). Bench-top testing of the stent designs revealed deployed stent lengths of 21.20 and 22.50 mm for the high-stress and low-stress stents, respectively. Furthermore, testing indicated that different inflation pressures were required to expand the stents to their designed and manufactured outer diameters of 5.0 mm (high-stress stent = 10 atm, low-stress stent = 8 atm; such variations in inflation pressures further emphasize the stiffness of the two designs). Stents were inflated to their respective pressures and maintained for approximately 30 seconds. Angiograms were performed to document stent post-deployment location, baseline diameter, and proper strut apposition (Figure 2). There were no significant differences in baseline diameters of the stent groups as measured from angiographic images. The implantation sites for the two stent designs were randomized.

Approximately 28 days post-implantation (28 ± 1 day), animals were anesthetized as described above and a final angiogram was obtained. The animals were euthanized with a bolus injection of pentobarbital (120 mg/kg) while still under general anesthesia and transported to the necropsy lab for tissue harvesting. During the necropsies, the stented arteries were located, flushed with phosphate buffered saline for 10 minutes, and fixed in situ by perfusion with 10% neutral buffered formalin for 10 minutes. The stented vessels were isolated, photographed, and transported to the Cardiovascular Pathology Laboratory

(Department of Veterinary Pathobiology, College of Veterinary Medicine and Biomedical Sciences, Texas A&M University) for processing.

Histomorphometric and Histopathologic Evaluation

Following tissue harvesting and removal of excess connective tissue, stented artery specimens were prepared for histological analysis. Prior to micro-CT acquisition, stented arteries were injected with a barium sulfate solution (0.56 g/mL) to ensure adequate contrast between the vessel lumen, stent struts, and surrounding arterial tissue. Barium-injected specimens were then dehydrated through graded alcohols, infiltrated with plastic embedding media (Technovit 7200, EXAKT Technologies, Inc., Oklahoma City, OK, USA), and polymerized.

Once the tissue was processed, micro-CT images of the stented arteries were acquired (HAWK-160XI, X-Tek Group, Inc., Santa Clara, CA, USA). Micro-CT scans were reconstructed (VGStudio MAX, v. 2.0, Volume Graphics, Heidelberg, Germany) for visualization and qualitative evaluation of stent structural integrity. Furthermore, 8-bit image stacks of the micro-CT scans were exported to conduct quantitative micro-CT measurements on the stented arteries (discussed below).

Following micro-CT scan acquisition, histological sections were prepared and analyzed. Briefly, plastic embedded specimens were cut with a diamond-coated band saw (EXAKT 300, EXAKT Technologies Inc.), and two sections from the middle region of each stent were prepared and micro-ground to a thickness of approximately 10 μm (EXAKT 400, EXAKT Technologies Inc.). For each stented artery, one section was stained with H&E to examine cellular type/quantity and fibrin deposition, while the other section was stained with Verhoeff van Gieson (VVG) elastin stain for injury scoring. Morphometric analysis was performed to quantify the areas inside the lumen, IEL, and EEL, and the neointimal thickness at each stent strut (Image-ProR Plus, v. 6.3, Media Cybernetics, Inc., Bethesda, MD, USA). Measurements allowed for calculation of intimal area (IEL area – lumen area), medial area (EEL area–IEL area), and percent stenosis {[1 (lumen area/IEL area)] × 100}. Furthermore, histopathologic analysis was carried out to quantify vessel injury {modification from (24–26); defined as the anatomic structure [e.g. IEL, medial layer, external elastic lamina (EEL)] penetrated or perforated by the stent strut}, inflammation [modification from (26–28)], residual erythrocyte distribution, residual erythrocyte state, presence of neovascular buds, fibrin deposition, and presence of multinucleated giant cells (MNGC). Note that all values in the histopathologic analysis ranged from 0 (absent/ minimal) to 4 (severe) and are discussed in detail elsewhere (29).

Novel quantitative micro-CT techniques were utilized to further assess the pathobiologic response (i.e. measure neointimal tissue area). These techniques allow for measurements of common morphological features of the stented arteries (e.g. lumen area, stented area, neointimal area) without the need for histological processing. As discussed above, image stacks of the micro-CT scans were exported from the reconstruction software and subsequently imported into a custom semi-automated Matlab (MathWorks) subroutine. Imaging processing techniques (e.g. thresholding, size exclusion) were applied to each micro-CT image (~1400 per scan; resolution ~20 μm) to separate the artery lumen and stents

struts. Knowing the resolution of the images allowed for calculation of the lumen area, while the area encompassed by the stent in each image was determined by fitting an ellipse (least-squares fit) to the outer edge of the stent struts. The neointimal area was calculated as the difference between the stent and lumen areas.

Following analysis of each image, the micro-CT images corresponding to the prepared histology slides (stained with VVG) from the middle of the stents were visually determined to allow for comparison of the two techniques. Briefly, independently determined measurements of the lumen areas were compared and a correction coefficient, defined as the ratio of the lumen areas as determined by micro-CT and histomorphometry, was calculated; note that a different correction coefficient was calculated for each specimen (0.79 ± 0.04), as differences in beam power and focal plane orientation varied amongst CT scans. It was assumed that the histomorphometric values were "correct" and thus the micro-CT measurements were adjusted to them. To verify that the correction coefficient held true for any region of the stented artery, independent morphometric measurements were carried out on the H&E stained histology slide and corresponding micro-CT image. The calculated correction coefficient for a given specimen was applied to the lumen area calculated from the micro-CT image, and the corrected value was then compared to the lumen area measured from the H&E histology slide. For all specimens measured, the average difference between the corrected micro-CT and histomorphometric lumen values was 0.24 mm^2 (avg. difference of 2.03%) with a difference never greater than 0.90 mm^2 (Fig. 6D). Following calculation and verification of the correction coefficient, analysis could be conducted on any region of the stented artery. In particular, quantitative micro-CT was carried out at the proximal and distal regions of the stented arteries. Micro-CT images in the stented region approximately 4.3 mm from the stent edges (herein, denoted as the proximal and distal regions) were analyzed and neointimal areas were determined. These specific locations were chosen as they allowed for proper evaluation of these regions, while ensuring that there was no artifact due to tissue prolapse at the edges as a result of harvesting and fixing of the tissue. It should be reiterated that the micro-CT scans were performed following tissue processing and embedding, thus there was no concern for tissue shrinkage to affect the correlation between histomorphometric and micro-CT values.

Statistical Analysis

Histomorphometric parameter values were calculated at each stent strut within a single micrograph, while morphometric values were determined from three measurements per micrograph (lumen, IEL, EEL area) or a measurement at each stent strut (neointimal thickness). Differences between stent groups were determined using the paired Student's t-test with $p < 0.05$ deemed statistically significant. All results are reported as mean $\pm$ standard error of the mean (SEM).

Results

Examination of the finite element analysis results reveals that the high-stress stent induces considerably larger circumferential stress values on the artery wall than the low-stress stent at diastolic pressure. On average, tensile circumferential stress values on the inner surface of

the artery models were approximately 20% larger in the high-stress stent than the low-stress stent in the stented region of the artery (Fig. 3A). Peak stress values of approximately 3100 kPa (> 13x larger than an unstented vessel at diastole) were observed for both the high-stress and low-stress stent; however, the high-stress stent subjected the artery to such large stress values over relatively diffuse areas of the stented region. Circumferential stress values > 2300 kPa covered > 86% of the artery wall. In contrast, the low-stress stent only induced such high stress at focal regions of the intimal surface that were directly adjacent to stent struts, with stress values > 2300 kPa only covering < 13% of the artery wall.

Both stent designs expanded the artery to approximately the same diameter and thus would be deemed clinically successful (i.e. the diameter of the artery at the implant site is greater than the diameter at the unstented region, and therefore, assuming a constant flow rate, blood flow would increase). Differences in radial displacement values between the two stent designs were minimal (average difference in the stented region ~ 70 μm at diastolic pressure). In general, regions of high stress were also the sites of the greatest radial displacement in the stented region (i.e. the highest radial displacements occurred where the stent struts contacted the artery wall). Overall, the high-stress stent design displaced the artery to a more uniform radial position than the low-stress stent (Fig. 3B). At locations where the high-stress stent was in contact with the artery wall, the artery was displaced approximately 0.71 mm in the radial direction. Note that radial displacements are in reference to the position of the lumen surface at diastolic pressure (i.e. a radial displacement of 0 mm indicates that there was no increase in lumen size). Furthermore, radial displacement values of > 0.63 mm occurred over > 94% of the inner surface of the stented region, with an average radial displacement of 0.67 mm. In contrast, the low-stress stent displaced the artery wall > 0.63 mm on < 33% of the inner surface, with an overall average radial displacement value of 0.60 mm.

All animals survived the implantation procedure. In total, 8 non-atherosclerotic pigs were used in this study, with 18 stents deployed [9 of each design (8 in iliac arteries, 1 in femoral artery); in one animal 2 stents of each design were implanted (1 in each of the iliac arteries, 1 in each of the femoral arteries) as the size and geometry of the vasculature allowed for multiple implantations]. It should be noted that in the animal where 2 stents were deployed on each side, the stents were implanted approximately 10 mm a part, and computational studies have indicated that this distance is sufficient to avoid any mechanical (solid or fluid) interaction between them (16, 30). There were no episodes of subacute stent thrombosis, and all of the stents remained patent prior to euthanasia, as observed under angiography.

Morphometry showed that intimal area was significantly greater in the high-stress stent group (Table 1; Fig. 4A; $p = 0.00008$). Intimal area values of 4.333 ± 0.303 and 1.599 ± 0.175 mm^2 were observed in the high-stress stent and low-stress stent groups, respectively; however, medial area was not significantly different between the groups (1.569 ± 0.162 vs. 1.349 ± 0.092 mm^2, respectively). Furthermore, the percentage of stenosis was also significantly greater in the high-stress stent group, with values of 23.598 ± 1.697 % and 15.643 ± 2.272 %, respectively (Fig. 4B; $p = 0.004$). In addition, examination of the neointimal thickness at each stent strut revealed a significantly greater thickness value for the struts in the high-stress stent group when compared to the low-stress stent group (Fig.

4C; $p = 0.0004$). The high-stress stent group had an average neointimal thickness value at each stent strut of 0.197 ± 0.020 mm, while the low-stress stent group had a value of 0.071 ± 0.016 mm. Qualitative analysis of the micrographs further confirmed this observation of greater neointimal thickness in the high-stress stent group (Fig. 5). It should be mentioned that morphometric values in the stented femoral artery specimens were not notably different from those in the iliac arteries (i.e. femoral artery values were not the maxima or minima morphometry values for the data range).

The quantitative micro-CT techniques provided further quantitative data of differences in the pathobiologic response following implantation of the two stents (Fig. 6). In particular, it allowed for examination of neointimal tissue and lumen areas at the proximal and distal regions of the stents (± 4.3 mm from the stent edge) and lumen areas in the non-stented regions (± 1 mm from the stent edge) without the need for histological processing. Examination of the micro-CT images at these locations again revealed a significant difference between the stent groups in the amount of neointimal tissue present. The proximal region of the high-stress stent group had a neointimal area value of 6.545 ± 0.557 mm^2, whereas the low-stress stent group had a value of 2.864 ± 0.254 mm^2 (Fig. 7A; $p = 0.0002$). Furthermore, analysis of the neointimal area at the distal regions of the stents showed a significant difference between the stent groups ($p = 0.004$), with values for the high-stress and low-stress stent groups of 6.542 ± 0.578 mm^2 and 3.229 ± 0.694 mm^2, respectively. In addition to differences in the amount of neointimal tissue present between the stent groups, variations in the neointimal area values at various locations (proximal, middle, and distal regions) within a given stent group were observed (Fig. 7B). For both stent designs, there were significant differences in the neointimal area when comparing the values at the proximal and distal regions to the values measured in the middle regions. However, the results were not significantly different when comparing the amount of neointimal tissue amongst the proximal and distal regions in each stent group. Finally, the high-stress stent group resulted in a significantly greater lumen area than the low-stress stent group in the proximal (14.087 ± 0.916 mm^2 vs. 9.369 ± 0.985 mm^2, $p = 0.00003$), middle (14.616 ± 1.010 mm^2 vs. 9.398 ± 0.885 mm^2, $p = 0.0004$), and distal (13.927 ± 1.074 mm^2 vs. 8.338 ± 1.231 mm^2, $p = 0.0007$) regions of the stented arteries (Fig. 7C). While the high-stress stent displaced the artery to a greater degree, examination of the non-stented regions (i.e., ~ 1 mm from the stented edges) revealed that both stents expanded the lumen to greater values. Lumen areas in the non-stented regions of the high-stress and low-stress stent groups were 10.6117 ± 0.885 mm^2 and 8.0483 ± 0.757 mm^2, respectively.

Histopathologic analysis revealed no significant differences in any measures between the stent groups (Table 1). Injury scores of 0.976 ± 0.024 and 0.901 ± 0.043 were observed in the high-stress stent and low-stress stent groups, respectively. In most cases, the stent struts were in contact, but not penetrating, the IEL (score equal to 1). Furthermore, inflammation, defined as the level of lymphohistiocytic aggregates, was minimal in both groups with a score of 1.010 ± 0.007 for the high-stress stent group and 1.031 ± 0.018 for the low-stress stent group. Peristrut hemorrhage was rarely observed in either group (RBC distribution score: high-stress stent = 0.034 ± 0.016, low-stress stent = 0.112 ± 0.044); however, if present, residual erythrocytes had a discoid morphology and showed no indication of

degeneration (RBC state score: high-stress stent = 0.063 ± 0.032, low-stress stent = 0.174 ± 0.081). Neovascular bud formations were not identified in any of the histopathological analysis for either group. Minimal fibrin deposition appeared in either group, although, while not statistically significant, greater deposition was observed in the high-stress stent group (1.110 ± 0.096) than the low-stress stent group (0.860 ± 0.123). Finally, MNGC were not frequently observed (high-stress stent = 0.192 ± 0.047, low-stress stent = 0.189 ± 0.058).

Discussion

This investigation used both computational and direct in vivo analysis to provide unique information on the role of solid biomechanics in the development of restenosis. Two stent designs (defined as the high and low-stress stents) were implanted in porcine external iliac or femoral arteries and analyzed using various integrative pathologic techniques. Furthermore, computational methods were utilized to analyze the biomechanical impact of these varying stent designs in an artery model that featured nonlinear strain-stiffening properties. Results indicate that the stent design that induced higher stress values on the artery wall lead to a more significant pathobiologic response as determined by the amount of neointimal hyperplasia.

To our knowledge, the data presented are the first to document stent-induced variations in the solid biomechanical environment with corresponding direct quantitative in vivo evidence of neointimal tissue growth (i.e. not angiographic clinical data). Both stent designs were constructed of the same material, deployed under the same conditions, and showed no significant difference in histopathologic response (Table 1). Differences between the stents where only observed in their biomechanical environments (Fig. 3) and associated amounts of neointimal tissue (Figs. 4, 5, and 7). Thus, we conclude that the resulting pathobiologic differences are a direct result of the mechanical loads placed on the artery wall, confirming the hypothesis that stents that induce a non-favorable biomechanical environment (i.e. subject the artery to higher, non-physiologic stresses) provoke a more aggressive pathobiological response.

Computational analysis has emerged as a valuable analysis and design tool for evaluation of implantable medical devices. Vascular stents have garnered much interest in this area, as the implantation of a stent is a highly complex mechanical process and the biomechanical interaction of the stent and artery is, as shown, important in the long-term success of the therapy. However, while many studies have developed sophisticated numerical methods to investigate stented artery biomechanics, few studies have directly applied their results to experimental or clinical data. As observed in this investigation, other computational studies have also indicated a strong correlation between stent-induced arterial wall stress and clinical angiographic restenosis data. Lally et al. (31) demonstrated that the NIR stent design (Boston Scientific, Maple Grove, MN, USA) induced much higher stresses than the S7 stent design (Medtronic, Minneapolis, MN, USA) on a generalized atherosclerotic artery model. Such results support clinical findings, as 6 month follow-up data of the two designs report restenosis rates of 19.0 and 10.1%, respectively. Berry et al. (32) evaluated the arterial wall mechanics and resulting short-term (7 days) pathobiologic response in a swine model of a prototype stent that provides a smoother transition in compliance at the edges of the stent

[termed compliance matching stent (CMS)]. Comparison of the computational results between the CMS and the commercially available Palmaz-Schatz designs indicated that the CMS reduced the circumferential wall stresses at the ends of the stent. The reduction in stress values was associated with minimal accumulation of thrombus and inflammatory cells when comparing in vivo results for the CMS (32) and Palmaz-Schatz designs (33). It is interesting to note that in our investigation the greatest amount of neointimal tissue was present at the proximal and distal regions of the two stent designs (Fig. 7), which agrees with clinical findings (34). These regions are where the highest gradients in wall stress were observed (Fig. 3), with the largest gradient, or compliance mismatch, occurring in the high-stress stent. This finding provides further evidence that a stent design that reduces the abrupt change in wall stress could reduce the amount of neointimal proliferation.

Explanations for the reasoning behind the differences in the observed pathobiologic response are directed at the alterations in the highly controlled and sensitive native biomechanical loading environment that is disrupted following stent implantation. As experimental studies have indicated, the vasculature adapts to changes in blood flow, sustained increases in blood pressure, and altered axial extension in such a manner as to restore the altered mechanical state (e.g. mean wall shear stress, circumferential and axial wall stress) to homeostatic levels [see review by Humphrey (35)]. Thus, it is reasonable to expect that following stent deployment the artery will remodel in such a way (neointimal hyperplasia) as to attempt to return the wall stresses to values prior to the interventional therapy. The greater the difference between the stent-induced and homeostatic wall stresses, the more aggressive the biological response, and in the case of this investigation, the higher degree of neointimal tissue. Such a statement is supported by a theoretical model proposed by Rachev et al. (36) that examined the stress-induced thickening of the arterial wall at regions near a stent. Results indicate that local arterial thickening is a remodeling process that occurs due to changes in the biomechanical environment to which the artery adapts. Furthermore, the model predicts that arterial thickening is greatest at regions where stress concentrations are the highest (i.e. where stress concentrations deviate the most from the homeostatic value). Garasic et al. (37) also developed a mathematical model to predict neointimal tissue post-stenting; however, their model is extremely limited by a lack of biological or mechanical rational that actively drives the model. Collectively, experimental and modeling data indicate that stent designs that subject the artery wall to lower stress values, or whose induced stress values deviate the least from homeostatic values, and still serve their clinical role (e.g. restore patent lumen) will have greater long-term success.

There are several limitations in this study that should be addressed. Firstly, the experimental results in an animal model do not fully capture the mechanisms as they occur in humans. As noted by Farb et al. (28), the pathobiologic response in porcine coronary models closely reflects those observed in human coronary arteries; however, the healing response in humans is of longer duration. Regardless, porcine models are commonly utilized for evaluation of vascular stents because their vascular anatomy is comparable to that in human, thus allowing use of catheters and devices employed clinically. Furthermore, there is a high degree of similarity between histopathologic responses by the porcine coronary model and human arteries after both balloon injury and stent placement (24, 38). Therefore, the porcine model is well accepted as a suitable restenosis model for evaluation of stent design. Secondly, the

stents were implanted in a non-diseased animal model. As this investigation was focused on evaluating the pathobiologic response between two stent designs that impose strikingly different biomechanical environments, inclusion of heterogeneous atherosclerotic plaques may have confounded direct comparison between stent groups (i.e. plaque morphology and composition would not be constant from animal to animal, or even vessel to vessel). Moreover, the differences in the stenoses would have limited the applicability of the computational analysis to the in vivo results, and would have required complex "patient"-specific computational models to be computed for each animal. Thirdly, our novel quantitative micro-CT techniques do not allow for evaluation of the histopathologic response throughout the entire stented artery. Thus, it is possible that specific pathologic findings might not have been accounted for in the analysis. While not presented, histopathologic evaluation was carried out along the entire length of a stented artery specimen (i.e. approximately 25 histology slides) with no significant difference in the analysis parameters exhibited in Table 1. Furthermore, in all histology slides examined (~ 325 stent struts) there was never a presence of large accumulations of macrophages and MNGC, eosinophils, and/or granulomatous tissues. Therefore, in the present study the novel quantitative micro-CT techniques provided a valuable and efficient analysis tool. Given the added value of this technique, future efforts to develop a completely automated algorithm that can evaluate intimal and lumen areas along the entire axial length (i.e., in each micro-CT image) would offer exceptional benefit in the pathobiological analysis of stents. Such work was beyond the scope of the work presented. Fourthly, we acknowledge that the mechanical environment differs between the iliac (femoral) and coronary arteries, with larger deformations (e.g. changes in curvature, axial twisting) reported for human iliacs (femorals) than coronaries [compare (39) and (40)]. Experimental magnetic resonance data indicates that iliac (femoral) deformations are quite similar between pigs and humans during hind limb extension and flexion [compare (39) and (41)] further supporting the translation of the presented data to humans. Fifthly, while some stents were deployed in the external femoral artery, it was assumed that the material properties and mechanical response post-stenting where identical between the iliac and femoral arteries. While vascular tissue material properties do vary along the vascular tree, whether or not they differ significantly between the porcine iliac and femoral arteries has not been reported. However, regardless of the strain-stiffening material properties employed in this investigation, the high-stress stent would still induce greater stresses on the arterial wall, as a result of higher radial displacements, than the low-stress stent. Finally, as with any computational modeling study, there are limitations with the computational techniques. Briefly, these limitations include characterizing the artery as a homogeneous, isotropic, hyperelastic material, neglecting the effects of residual strain, not including arterial bending or torsion, and not modeling the stent balloon expansion process. Such limitations have been discussed in detail elsewhere (14, 18). It should be noted that inclusion of these features would have been computationally, extremely demanding and would, most likely, not have affected the relative comparison between the two stent designs (high-stress stent would still impose greater stress values).

Designing the next generation of vascular stents will require collaborative efforts between clinical interventionalists, biomechanicians, pathologists, cellular biologists, polymer

chemists, and manufacturing engineers, to name a few. The work presented constitutes a major effort in characterizing the mechanical impact of vascular stenting and offers information on specific design criteria to reduce the pathobiologic response. However, there are other design criteria that are valuable and should be considered. In the past 6-7 years, application of cytostatic pharmaceutical agents to stents (i.e. DES) has gained notoriety (42, 43). Despite their shortcomings (as mentioned above) the technology does offer promise to the interventional therapy. It is likely that the most successful stents of tomorrow will combine intelligent biomechanics with advancements in drug-elution. In addition, advancements in high-resolution imaging techniques (e.g. CT, magnetic resonance imaging, intravascular ultrasound, optical coherence tomography) will allow visualization and characterization of the diseased vasculature prior to intervention. Such information will allow for the development of patient-specific computational models that allow for mechanical, durability, and efficacy testing [as discussed for endovascular devices by Zarins and Taylor (44)], and thus ensure that the most optimal stent is implanted (i.e. patient-specific stenting).

From a clinical perspective, the data presented emphasize a critical aspect of reducing chronic trauma to the artery wall that will likely increase the success rate of this interventional therapy. While our data reveal that the high-stress stent group resulted in a significantly larger final lumen area (Table 1, Fig. 7), both stent designs were effective at increasing the final lumen area relative to the unstented artery, – even at 28 days. Both stents resulted in stented segments that were less resistive than the native healthy vessel, and stent migration was never observed. Thus, the stents investigated in this study were clinically successful. Such information further emphases the importance that the stent design that results in the largest final lumen diameter is not required, and can cause unnecessary trauma to the artery wall that can result in severe pathologic consequences, [i.e., IEL/EEL rupture, and restenosis; (22)]. Rather the stent that restores a patent lumen, but minimizes unnecessary trauma is a better choice. For example, if a clinician had the option of implanting one of two stent designs, both of which meet all clinical criteria (e.g. restore patent lumen, lack of short- and long-term stent thrombosis, provide adequate scaffolding, structurally sound, etc.), the data suggest that the stent design that induces less stress on the artery wall is likely to reduce neointimal tissue formation, and possible restenosis formation. While the data only support this statement for the porcine iliac (femoral) arteries, it is probable that the results can be extended to all vascular beds (e.g. coronaries, carotids, superficial femorals, cerebrals, etc.); however, it should be emphasized that each region of the vasculature has different requirements for successful treatment.

In conclusion, this study provides valuable insight into the role that biomechanics can play in the development of neointimal tissue following vascular stent implantation. The results not only provide information that is directly applicable to commercially available designs, but also yield information about specific design criteria and considerations that should be made when designing the next iteration of stents. In addition, the novel integrative pathology techniques presented (e.g. quantitative micro-CT) provide a means of extracting highly detailed quantitative data from the pathobiologic response of vascular stents, and such methods are applicable to examine other implantable medical devices.

Acknowledgments

Abbreviations

BMS	bare-metal stents
CSA	cross-sectional area
CT	computed tomography
DES	drug-eluting stents
EEL	external elastic lamina
FE	finite element
H&E	hematoxylin and eosin
IEL	internal elastic lamina
MGNC	multi-nucleated giant cells
VVG	Verhoeff van Gieson

References

1. Kastrati A, Mehilli J, Dirschinger J, et al. Restenosis after coronary placement of various stent types. Am J Cardiol. 2001; 87(1):34–39. [PubMed: 11137830]

2. Serruys PW, Kutryk MJ, Ong AT. Coronary-artery stents. N Engl J Med. 2006; 354(5):483–495. [PubMed: 16452560]

3. Joner M, Finn AV, Farb A, et al. Pathology of drug-eluting stents in humans: delayed healing and late thrombotic risk. J Am Coll Cardiol. 2006; 48(1):193–202. [PubMed: 16814667]

4. Duda SH, Bosiers M, Lammer J, et al. Drug-eluting and bare nitinol stents for the treatment of atherosclerotic lesions in the superficial femoral artery: long-term results from the SIROCCO trial. J Endovasc Ther. 2006; 13(6):701–710. [PubMed: 17154704]

5. Nebeker JR, Virmani R, Bennett CL, et al. Hypersensitivity cases associated with drug-eluting coronary stents: a review of available cases from the Research on Adverse Drug Events and Reports (RADAR) project. J Am Coll Cardiol. 2006; 47(1):175–181. [PubMed: 16386683]

6. Lloyd-Jones D, Adams R, Carnethon M, et al. Heart disease and stroke statistics--2009 update: a report from the American Heart Association Statistics Committee and Stroke Statistics Subcommittee. Circulation. 2009; 119(3):480–486. [PubMed: 19171871]

7. Edelman ER, Rogers C. Pathobiologic responses to stenting. Am J Cardiol. 1998; 81(7A):4E–6E.

8. Duraiswamy N, Jayachandran B, Byrne J, et al. Spatial distribution of platelet deposition in stented arterial models under physiologic flow. Ann Biomed Eng. 2005; 33(12):1767–1777. [PubMed: 16389525]

9. Robaina S, Jayachandran B, He Y, et al. Platelet adhesion to simulated stented surfaces. J Endovasc Ther. 2003; 10(5):978–986. [PubMed: 14656171]

10. Kroll MH, Hellums JD, McIntire LV, et al. Platelets and shear stress. Blood. 1996; 88(5):1525–1541. [PubMed: 8781407]

11. Moazzam F, DeLano FA, Zweifach BW, et al. The leukocyte response to fluid stress. Proc Natl Acad Sci U S A. 1997; 94(10):5338–5343. [PubMed: 9144238]

12. Siow RC, Mallawaarachchi CM, Weissberg PL. Migration of adventitial myofibroblasts following vascular balloon injury: insights from in vivo gene transfer to rat carotid arteries. Cardiovasc Res. 2003; 59(1):212–221. [PubMed: 12829192]

13. Li L, Couse TL, Deleon H, et al. Regulation of syndecan-4 expression with mechanical stress during the development of angioplasty-induced intimal thickening. J Vasc Surg. 2002; 36(2):361–370. [PubMed: 12170195]

14. Bedoya J, Meyer CA, Timmins LH, et al. Effects of stent design parameters on normal artery wall mechanics. J Biomech Eng. 2006; 128(5):757–765. [PubMed: 16995763]

15. Timmins LH, Meyer CA, Moreno MR, et al. Mechanical modeling of stents deployed in tapered arteries. Ann Biomed Eng. 2008; 36(12):2042–2050. [PubMed: 18846425]

16. Timmins LH, Meyer CA, Moreno MR, et al. Effects of stent design and atherosclerotic plaque composition on arterial wall biomechanics. J Endovasc Ther. 2008; 15(6):643–654. [PubMed: 19090628]

17. Lemos PA, Moulin B, Perin MA, et al. Randomized evaluation of two drug-eluting stents with identical metallic platform and biodegradable polymer but different agents (paclitaxel or sirolimus) compared against bare stents: 1-year results of the PAINT trial. Catheter Cardiovasc Interv. 2009; 74(5):665–673. [PubMed: 19670303]

18. Timmins LH, Moreno MR, Meyer CA, et al. Stented artery biomechanics and device design optimization. Med Biol Eng Comput. 2007; 45(5):505–513. [PubMed: 17375345]

19. Bosiers M, de Donato G, Deloose K, et al. Does free cell area influence the outcome in carotid artery stenting? Eur J Vasc Endovasc Surg. 2007; 33(2):135–141. discussion 142–133. [PubMed: 17097897]

20. Chuong CJ, Fung YC. Compressibility and constitutive equation of arterial wall in radial compression experiments. J Biomech. 1984; 17(1):35–40. [PubMed: 6715386]

21. Han HC, Fung YC. Longitudinal strain of canine and porcine aortas. J Biomech. 1995; 28(5):637–641. [PubMed: 7775500]

22. Farb A, Weber DK, Kolodgie FD, et al. Morphological predictors of restenosis after coronary stenting in humans. Circulation. 2002; 105(25):2974–2980. [PubMed: 12081990]

23. Indolfi C, Torella D, Coppola C, et al. Rat carotid artery dilation by PTCA balloon catheter induces neointima formation in presence of IEL rupture. Am J Physiol Heart Circ Physiol. 2002; 283(2):H760–767. [PubMed: 12124225]

24. Schwartz RS, Edwards WD, Bailey KR, et al. Differential neointimal response to coronary artery injury in pigs and dogs. Implications for restenosis models. Arterioscler Thromb. 1994; 14(3):395–400. [PubMed: 8123644]

25. Verheye S, Salame MY, Robinson KA, et al. Short- and long-term histopathologic evaluation of stenting using a self-expanding nitinol stent in pig carotid and iliac arteries. Catheter Cardiovasc Interv. 1999; 48(3):316–323. [PubMed: 10525238]

26. Kornowski R, Hong MK, Tio FO, et al. In-stent restenosis: contributions of inflammatory responses and arterial injury to neointimal hyperplasia. J Am Coll Cardiol. 1998; 31(1):224–230. [PubMed: 9426044]

27. Virmani R, Farb A. Pathology of in-stent restenosis. Curr Opin Lipidol. 1999; 10(6):499–506. [PubMed: 10680043]

28. Farb A, Sangiorgi G, Carter AJ, et al. Pathology of acute and chronic coronary stenting in humans. Circulation. 1999; 99(1):44–52. [PubMed: 9884378]

29. Silva GV, Fernandes MR, Madonna R, et al. Comparative healing response after sirolimus- and paclitaxel-eluting stent implantation in a pig model of restenosis. Catheter Cardiovasc Interv. 2009; 73(6):801–808. [PubMed: 19309735]

30. LaDisa JF Jr, Olson LE, Guler I, et al. Circumferential vascular deformation after stent implantation alters wall shear stress evaluated with time-dependent 3D computational fluid dynamics models. J Appl Physiol. 2005; 98(3):947–957. [PubMed: 15531564]

31. Lally C, Dolan F, Prendergast PJ. Cardiovascular stent design and vessel stresses: a finite element analysis. J Biomech. 2005; 38(8):1574–1581. [PubMed: 15958213]

32. Berry JL, Manoach E, Mekkaoui C, et al. Hemodynamics and wall mechanics of a compliance matching stent: in vitro and in vivo analysis. J Vasc Interv Radiol. 2002; 13(1):97–105. [PubMed: 11788701]

33. Rolland PH, Charifi AB, Verrier C, et al. Hemodynamics and wall mechanics after stent placement in swine iliac arteries: comparative results from six stent designs. Radiology. 1999; 213(1):229–246. [PubMed: 10540667]

34. Hoffmann R, Mintz GS, Dussaillant GR, et al. Patterns and mechanisms of in-stent restenosis. A serial intravascular ultrasound study. Circulation. 1996; 94(6):1247–1254. [PubMed: 8822976]

35. Humphrey JD. Vascular adaptation and mechanical homeostasis at tissue, cellular, and sub-cellular levels. Cell Biochem Biophys. 2008; 50(2):53–78. [PubMed: 18209957]

36. Rachev A, Manoach E, Berry J, et al. A model of stress-induced geometrical remodeling of vessel segments adjacent to stents and artery/graft anastomoses. J Theor Biol. 2000; 206(3):429–443. [PubMed: 10988028]

37. Garasic JM, Edelman ER, Squire JC, et al. Stent and artery geometry determine intimal thickening independent of arterial injury. Circulation. 2000; 101(7):812–818. [PubMed: 10683357]

38. Schwartz RS, Murphy JG, Edwards WD, et al. Restenosis after balloon angioplasty. A practical proliferative model in porcine coronary arteries. Circulation. 1990; 82(6):2190–2200. [PubMed: 2146991]

39. Choi G, Shin LK, Taylor CA, et al. In vivo deformation of the human abdominal aorta and common iliac arteries with hip and knee flexion: implications for the design of stent-grafts. J Endovasc Ther. 2009; 16(5):531–538. [PubMed: 19842734]

40. Ding Z, Zhu H, Friedman MH. Coronary artery dynamics in vivo. Ann Biomed Eng. 2002; 30(4): 419–429. [PubMed: 12085995]

41. Karanian, JW.; Lopez, O.; Rad, D., et al. FDA/NHLBI/NSF Workship on Computer Methods for Cardiovascular Devices: The Integration of Nonclinical and Computer Models. Rockville, MD: 2010. Characterization of Vasculr Implant Sites by Localized Quantitative Mapping of Vascular Geometry.

42. Grines CL. Off-label use of drug-eluting stents putting it in perspective. J Am Coll Cardiol. 2008; 51(6):615–617. [PubMed: 18261679]

43. Maisel WH. Unanswered questions--drug-eluting stents and the risk of late thrombosis. N Engl J Med. 2007; 356(10):981–984. [PubMed: 17296826]

44. Zarins CK, Taylor CA. Endovascular device design in the future: transformation from trial and error to computational design. J Endovasc Ther. 2009; 16 (Suppl 1):I12–21. [PubMed: 19317584]
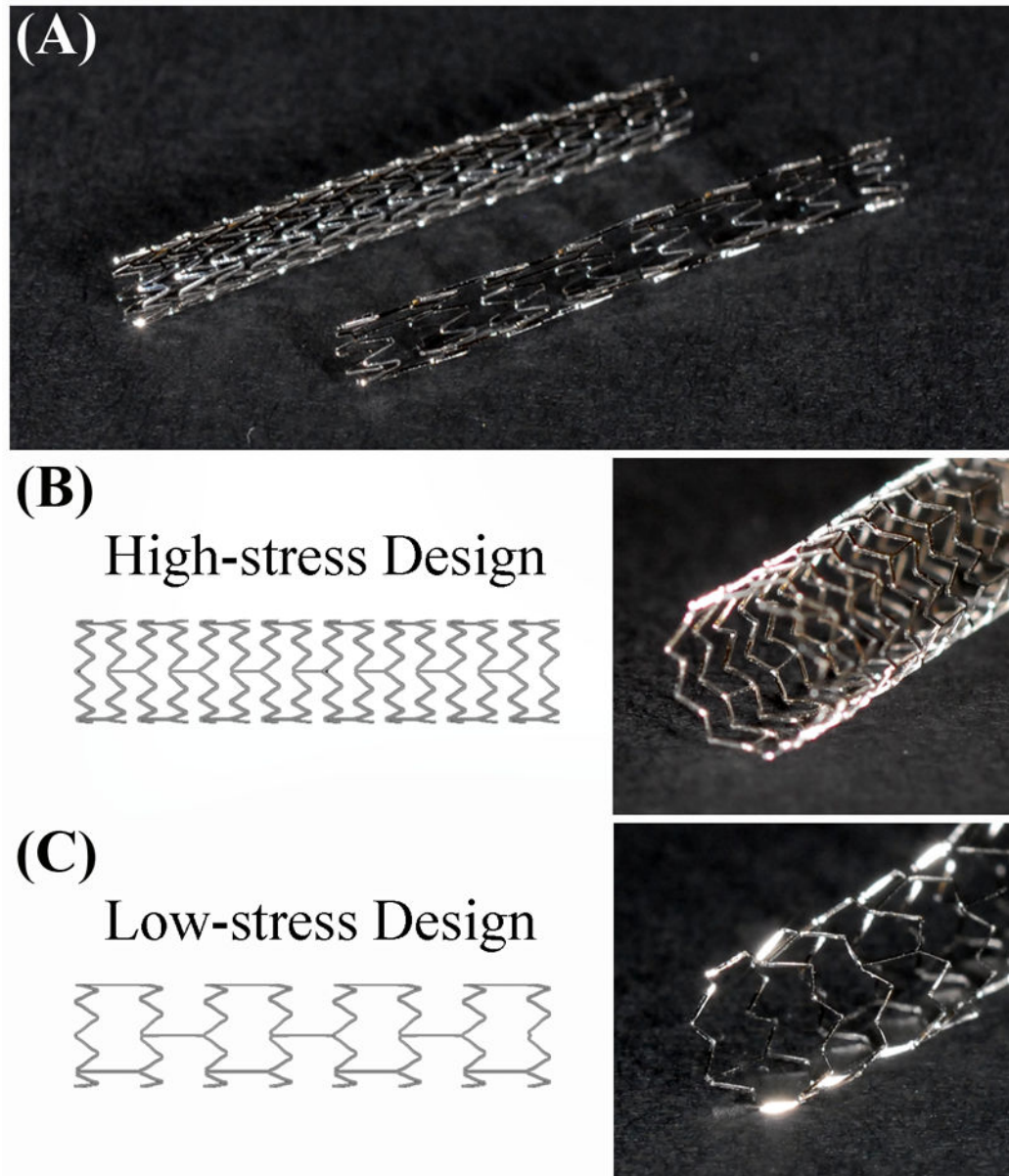
Figure 1.
Vascular stent designs for the in vivo study and computational modeling. (A) Laser cut stent designs prior to attachment on balloon catheter system for implantation. (B) Deployed high-stress stent (left: finite element model, right: laser cut design). (C) Deployed low-stress stent.
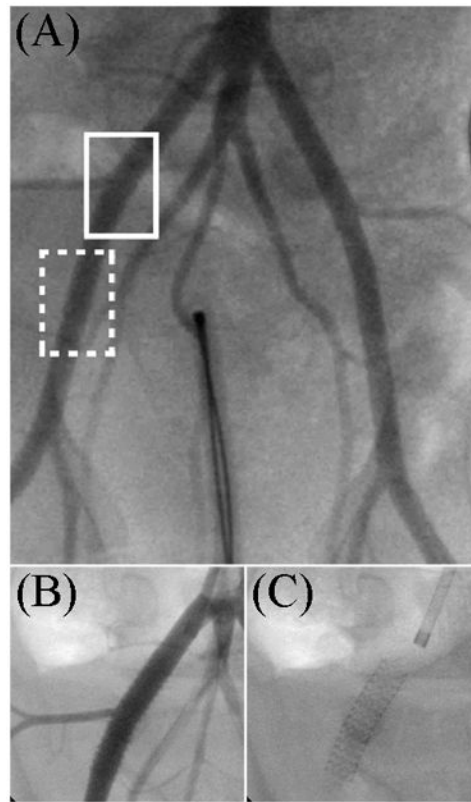
Figure 2.
Angiographic images from a stent implantation procedure. (A) Image of the hind limb region of prior to stent implantation (white solid box denotes the approximate location of implant site on the right iliac artery, white dotted box denotes the approximate location of the implant site in the right femoral artery). Following stent deployment, the implant sites were imaged with (B) and without (C) the injection of contrast media to examine the absence of subacute stent thrombosis and proper stent deployment and strut apposition, respectively.
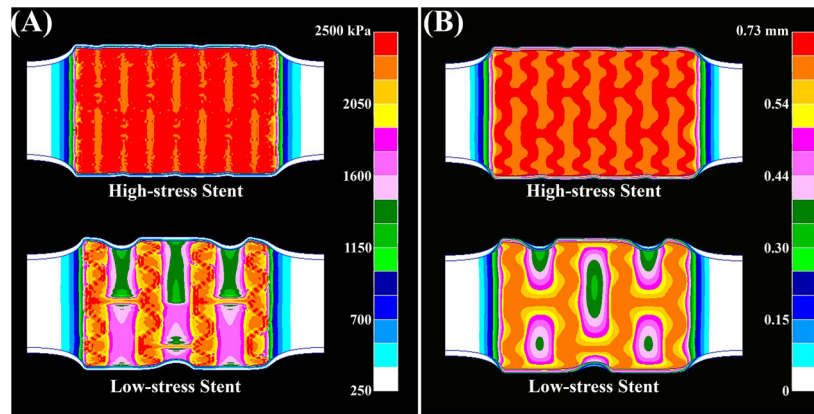
Figure 3.
(A) Circumferential (hoop) stress fields on the intimal surface of the artery wall at diastolic pressure. The high-stress stent imposed extremely high stresses (> 2300 kPa) across large regions of the artery, while the low-stress stent only induced such values at focal regions. On average, the low-stress stent induced stress values that were ~ 450 kPa lower than the high-stress stent design. (B) Radial displacement distributions on the intimal surface of the artery wall at diastolic pressure. As the high-stress stent induced the highest stresses on the artery wall, it also displaced the artery to a greater radial position than the low-stress stent design. Note '0' represents the inner radial position of the artery wall at diastolic pressure when no stent is present.
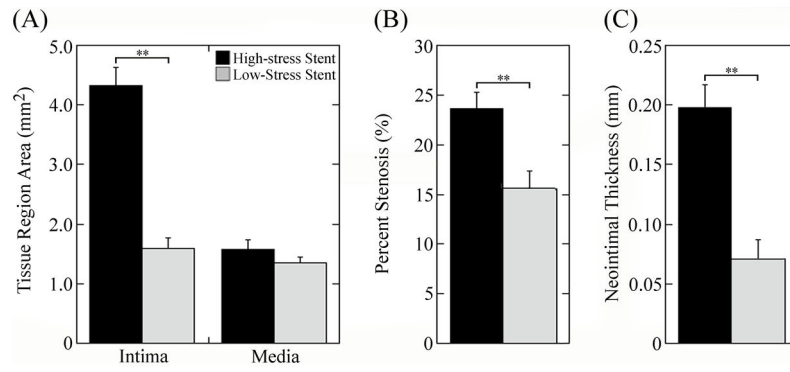
Figure 4.
Results from morphometric analysis. (A) Areas of intimal (IEL area - lumen area) and medial (EEL area – IEL area) regions. (B) Percent stenosis [1–(lumen area/IEL area) × 100]. (C) Neointimal thickness at stent struts. Data are means ± SEM of 18 tissue samples (9 per stent group). Significant differences ($p < 0.01$) are denoted by double asterisks.
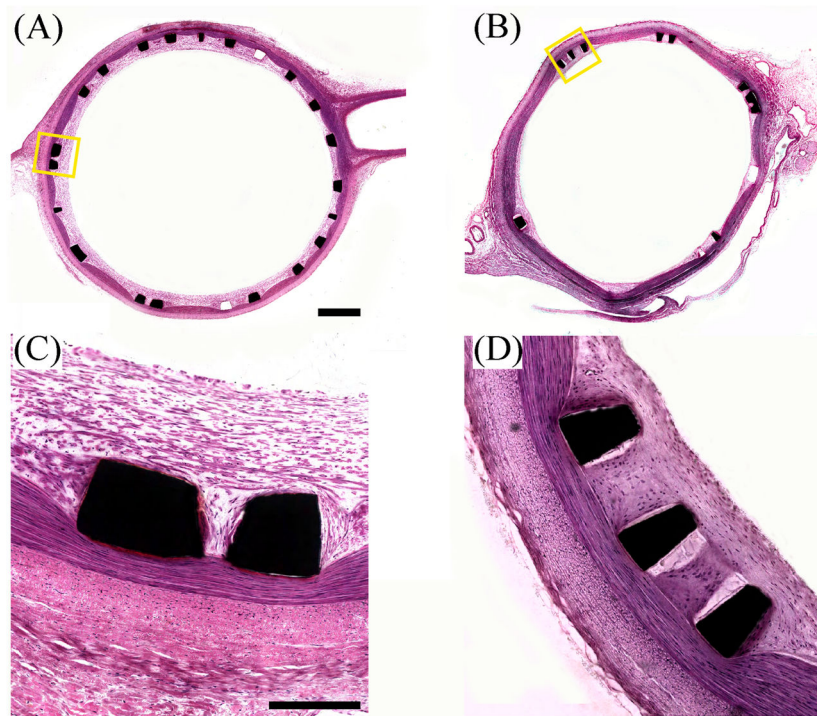
Figure 5.
Representative photomicrographs of plastic embedded stented vascular cross sections from the same animal stained with hematoxylin and eosin (thickness ~ 10 μm). Significant neointimal growth is observed at the struts of the high-stress stent (A, C; neointimal thickness = 0.107 ± 0.006), while minimal tissue growth is observed on the low-stress stent (B, D; neointimal thickness = 0.039 ± 0.007). Low magnification (A, B; scale bar = 5 mm), high magnification (C, D; scale bar = 250 μm).
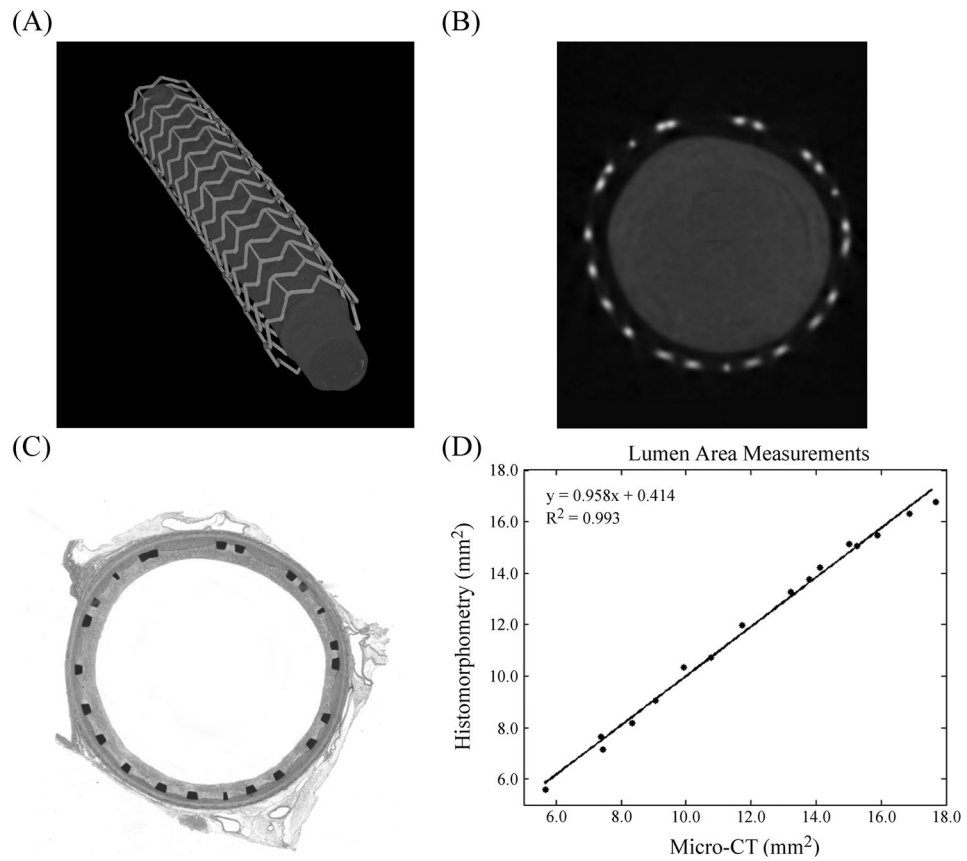
Figure 6.
Quantitative micro-CT analysis techniques and results. (A) Representative micro-CT rendering of a stented vessel with barium sulfate solution injected into the lumen. (B, C) Micro-CT axial slice and corresponding H&E stained micrograph from the middle region of a stented artery. (D) Comparison of the lumen areas as calculated by either quantitative micro-CT ("correction coefficient" applied) or histomorphometry (i.e. under light microscopy) to determine the accuracy of the data obtained from analyzing the micro-CT images. Note a regression line denoted by the equation $y = x$ would indicate an identical agreement between the two techniques.
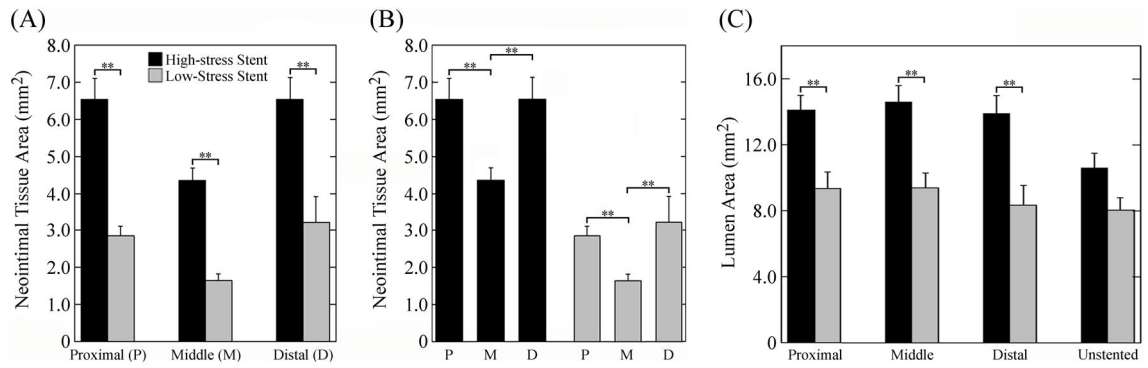
Figure 7.
Neointimal and lumen area values from the proximal, middle, and distal regions of the stented arteries. (A) Neointimal area amongst stent groups (high-stress vs. low-stress). (B) Neointimal area at different vessel locations within a stent group (proximal/distal vs. middle). (C) Lumen area amongst stent groups and in unstented regions (i.e., ~ 1 mm from the stent edges). Data are means ± SEM of 16 tissue samples (8 per stent group). Significant differences ($p < 0.01$) are denoted by double asterisks.

Author Manuscript

Author Manuscript

Author Manuscript

Author Manuscript

Table 1

Morphometric Values of Implanted Stent Design.

Morphometric Parameter	High-Stress Stent	Low-Stress Stent	p-value
Lumen Area (mm^2)	14.294 ± 0.839	9.064 ± 0.792	0.00007
IEL Area (mm^2)	18.627 ± 0.893	10.663 ± 0.793	0.00001
EEL Area (mm^2)	20.195 ± 1.006	12.012 ± 0.811	0.000008
Intimal Area (mm^2)	4.333 ± 0.303	1.599 ± 0.175	0.00008
Percent Stenosis	23.598 ± 1.697	15.643 ± 2.272	0.004
Media Area (mm^2)	1.569 ± 0.162	1.349 ± 0.092	0.120
Neointimal Thickness (mm)	0.197 ± 0.020	0.071 ± 0.016	0.0004

Table 2

Histopathologic Analysis of Implanted Stent Design.

Histopathologic Parameter	High-Stress Stent	Low-Stress Stent	p-value
Injury	0.976 ± 0.024	0.901 ± 0.043	0.107
Inflammation	1.010 ± 0.007	1.031 ± 0.018	0.175
RBC Distribution	0.034 ± 0.016	0.112 ± 0.044	0.079
RBC Stale	0.063 ± 0.032	0.174 ± 0.081	0.137
Neovascular Buds	0.000 ± 0.000	0.000 ± 0.000	N/A
Fibrin Deposition	1.110 ± 0.096	0.860 ± 0.123	0.063
MGNCs	0.192 ± 0.047	0.189 ± 0.058	0.488